Nonvolatile Manipulating Magnetic and Topological Properties in Sliding h-BN Capped $MnBi_2Te_4$

Xuqi Li[1†], Haidan Sang[1†], Yu Zhang[1], Hong Xu[1], Shifei Qi[1,2*], and Zhenhua Qiao[2*]

[1]*College of Physics and Hebei Advanced Thin Film Laboratory, Hebei Normal University, Shijiazhuang 050024, China*
[2]*International Center for Quantum Design, Hefei National Laboratory for Physical Sciences at Microscale, Chinese Academy of Sciences Key Laboratory of Strongly-Coupled Quantum Matter Physics, and Department of Physics, University of Science and Technology of China, Hefei 230026, China*

(Received 25 March 2025; accepted manuscript online 26 May 2025)

Interlayer antiferromagnetic coupling, small magnetic anisotropy, and low air stability of the intrinsic magnetic topological insulator $MnBi_2Te_4$ have been critical bottlenecks to the future application of the quantum anomalous Hall effect (QAHE) at zero magnetic field. In this study, we propose a scheme to utilize capped sliding van der Waals materials to effectively modulate the magnetic and topological properties of $MnBi_2Te_4$. Our results demonstrate that the h-BN/$MnBi_2Te_4$/h-BN heterostructure, constructed by sliding ferroelectric h-BN bilayer and $MnBi_2Te_4$, not only realizes a transition from interlayer antiferromagnetic to ferromagnetic coupling but also significantly enhances the out-of-plane magnetism and air stability of $MnBi_2Te_4$. Moreover, the above magnetic properties can be further improved by tuning the interlayer distance between h-BN and $MnBi_2Te_4$. Additionally, the obtained band structures and topological properties clearly support that the h-BN/$MnBi_2Te_4$/h-BN heterostructure can harbor the QAHE with a Chern number of $C = 1$. This work provides a new and nonvolatile modulation approach to achieve high-temperature and high-precision QAHE at zero magnetic field.

DOI: 10.1088/0256-307X/42/7/070709 CSTR: 32039.14.0256-307X.42.7.070709

Quantum anomalous Hall effect (QAHE), characterized by quantized Hall resistance and vanishing longitudinal resistance in the absence of an external magnetic field, offers new potential for applications in dissipationless or low-power electronic devices.[1–3] The theoretical realization of QAHE was initially proposed by Haldane through his honeycomb lattice model.[4] Subsequently, extensive efforts have been made to seek novel systems capable of realizing QAHE.[5–31] The emergence of strong three-dimensional topological insulators (TIs) has accelerated the realization of QAHE due to their strong spin–orbit coupling (SOC),[32,33] and QAHE was first observed in magnetic-element-doped TIs at an ultralow temperature of about 30 mK.[34] Despite the great breakthrough, the random distribution of magnetic dopants in TIs has been identified as a critical factor limiting the operation temperature to ultralow values. Although QAHE has also been successfully achieved in various other systems, including Te-based heterostructures composed of Cr-doped ZnTe magnetic semiconductors and $(Bi,Sb)_2Te_3$,[35] and more recently in intrinsic magnetic TI $MnBi_2Te_4$,[36–38] twisted graphene,[39] and transition-metal dichalcogenides,[40] achieving high-temperature QAHE at zero magnetic field remains elusive.

Due to homogeneous magnetic ordering and a large predicted magnetic exchange gap, $MnBi_2Te_4$ is considered an ideal platform for realizing high-temperature QAHE and axion insulator states.[41–43] In 2020, a nearly quantized Hall resistance of $R_{yx} = 0.97h/e^2$ was observed in 5-septuple-layer (5-SL) $MnBi_2Te_4$ films at 1.4 K at zero magnetic field. A more precise Hall resistance of $R_{yx} = 0.998h/e^2$ was achieved by increasing the perpendicular magnetic field to 2.5 T.[36] Subsequently, Ge *et al.* reported that the quantized Hall resistance of $R_{yx} = 0.98h/e^2$ was attainable in 7-SL $MnBi_2Te_4$ films at 1.9 K using a back gate of 6.5 V, and this plateau persisted at 45 K with $R_{yx} = 0.904h/e^2$.[44] Remarkably, similar QAHE was also observed in 8-SL $MnBi_2Te_4$ films at 1.9 K under an external magnetic field, demonstrating that ferromagnetic (FM) order is crucial for quantizing the Hall resistance, as the magnetic moments align with the applied external magnetic field. Furthermore, the enhanced observation temperature and precision of QAHE in $MnBi_2Te_4$ films under an external magnetic field are primarily attributed to the suppression of magnetic fluctuations due to improved magnetic anisotropy induced by the external magnetic field.[44] Therefore, in order to realize high-temperature and high-precision QAHE in $MnBi_2Te_4$ films at zero magnetic field, interlayer antiferromagnetic (AFM) coupling and small magnetic anisotropy are two key obstacles. It has also been experimentally observed that $MnBi_2Te_4$ films are prone to degrade under ambient conditions, and the magnetization M_s of the sample decreases significantly after being exposed to air for a couple of days.[42] Finding an effective way to protect this material under ambient conditions is also vital for its future

†These authors contributed equally to this work.
*Corresponding authors. Email: qisf@hebtu.edu.cn; qiao@ustc.edu.cn
© 2025 Chinese Physical Society and IOP Publishing Ltd. All rights, including for text and data mining, AI training, and similar technologies, are reserved.

applications.

Recent studies have shown that interlayer magnetic coupling in $MnBi_2Te_4$ is influenced by the d-orbital occupation of transition metals. An effective strategy for achieving interlayer FM includes stacking van der Waals (vdW) materials with different d-orbital occupations, such as $MnBi_2Te_4/V(Eu)Bi_2Te_4$[45,46] and $CrI_3/MnBi_2Te_4$.[47] Additionally, p-type element doping in a specific SL of $MnBi_2Te_4$ has been explored as a more direct approach to manipulate interlayer FM.[48] However, element doping might potentially compromise sample quality due to increased defect density and disorder. Given that $MnBi_2Te_4$ is a two-dimensional (2D) vdW magnetic material, an external electric field can effectively modulate carrier concentration, orbital occupation, and electronic structure, potentially affecting magnetic properties, including interlayer magnetic exchange coupling and magnetic anisotropy.[49,50] An external electric field can also break its inversion symmetry, lead to Rashba SOC, and produce nontrivial topological effects in 2D vdW materials. For instance, a previous theoretical study confirmed that an external electric field can significantly increase the magnetic anisotropy energy (MAE) of mono-SL $MnBi_2Te_4$ due to enhanced SOC induced by the external electric field. However, modulating the interlayer magnetic coupling and magnetic anisotropy of multi-SL $MnBi_2Te_4$ films through an external electric field is particularly intriguing, given the absence of topological properties in the mono-SL film.[49] A recent experimental study revealed that an external electric field only induced a magnetic phase transition from A-type AFM to tilted A-type AFM in multi-SL $MnBi_2Te_4$ films.[50] This is because an external electric field cannot exclusively alter the d-electron occupation in one specific SL without affecting others. Furthermore, the external electric field represents a volatile modulation method, meaning the modulated properties vanish when the field is removed. Consequently, there is a need for a nonvolatile electric modulation strategy to achieve interlayer FM coupling, enhance magnetic anisotropy, and protect the air stability of multi-SL $MnBi_2Te_4$ films.

In this study, we propose a method to modulate the magnetic and topological properties of $MnBi_2Te_4$ using sliding vdW materials. It is first demonstrated that the h-BN/$MnBi_2Te_4$/h-BN heterostructure, formed by a sliding ferroelectric (SFE) h-BN bilayer and a 2-SL $MnBi_2Te_4$ layer, can realize interlayer FM coupling and notably enhance both the out-of-plane magnetic stability and the air stability of $MnBi_2Te_4$. Additionally, our results show that applying compressive strain along the z-axis not only further strengthens the interlayer FM coupling but also increases the out-of-plane magnetic stability. The intrinsic mechanism behind the interlayer FM coupling can be attributed to the redistribution of d-orbital occupation of Mn ions between different superlattice layers, facilitating transition channels between the t_{2g} and e_g orbitals. Lastly, the calculated band structures and topological properties clearly support that the h-BN/$MnBi_2Te_4$/h-BN heterostructure can harbor QAHE with a nontrivial band gap and a Chern number of $C = 1$. This research presents a new and nonvolatile method to achieve high-temperature and high-precision QAHE at zero magnetic field and also suggests a nonvolatile approach to controlling the magnetic properties of 2D vdW A-type AFM materials.

Our first principles calculations were performed by the Vienna *ab initio* simulation package (VASP).[51,52] In the calculations, the generalized gradient approximation (GGA) of Perdew–Burke–Ernzerhof type was used to treat the exchange correlation interaction.[53] The experimental lattice constants for $MnBi_2Te_4$, $a = b = 4.334$ Å, were used.[54] To construct a commensurate interface, the primitive cell of $MnBi_2Te_4$ was matched to a $\sqrt{3}\times\sqrt{3}$ supercell of monolayer h-BN, which has an in-plane lattice constant of $a = b = 2.512$ Å. This results in an effective lattice constant of 4.351 Å for the h-BN supercell. The in-plane lattice mismatch was then calculated as

$$\text{Mismatch} = \frac{a_{\text{BN}}^{\sqrt{3}\times\sqrt{3}} - a_{\text{MBT}}}{a_{\text{MBT}}} \times 100\%$$

where $a_{\text{BN}}^{\sqrt{3}\times\sqrt{3}}$ is the effective lattice constant of the $\sqrt{3}\times\sqrt{3}$ supercell of h-BN, and a_{MBT} is the in-plane lattice constant of $MnBi_2Te_4$. Substituting the values gives a mismatch of approximately 0.39%. The heterostructure was constructed by fixing the lattice constant to that of $MnBi_2Te_4$, resulting in an extremely small compressive strain on the h-BN layer. To account for vdW interactions between adjacent layers of the heterostructure systems, we employed the zero-damping DFT-D3 method.[55] Full optimization of all internal atomic coordinates within the researched heterostructure systems was achieved. During the structural relaxation process, atomic positions were adjusted until the Hellmann–Feynman forces on each atom were below 0.02 eV/Å. The kinetic energy cutoff was set at 450 eV and a 20 Å vacuum buffer layer was included to prevent interactions between periodic images. Brillouin zone sampling was executed using Γ-centered 9×9×1 k mesh. Both SOC[56] and vdW interactions were included in all calculations. The GGA+U approach was employed to handle electron correlation effects in the unpaired 3d orbitals of Mn atoms, with a Hubbard $U_{\text{eff}} = 5.34$ eV, as previously reported.[57] Based on the above employed methods and parameters, band structure and magnetic properties, including interlayer magnetic coupling and MAE in 2-SL $MnBi_2Te_4$, have been correctly reproduced, as will be presented in the following. To explore topological properties, we constructed maximally localized Wannier functions to compute Berry curvature and anomalous Hall conductivity of the tight-binding model's Hamiltonian using the Wannier90 and WannierTools packages.[58,59]

As stated above, interlayer AFM coupling, small magnetic anisotropy, and low air stability of $MnBi_2Te_4$ present significant challenges for the future application of QAHE. Firstly, to protect the air stability of $MnBi_2Te_4$, as depicted in Fig. 1(a), an h-BN bilayer is used to encapsulate $MnBi_2Te_4$, as h-BN has been widely applied as a protective layer in various electronic devices.[60,61] For instance, experimental studies have demonstrated that

h-BN/phosphorene/h-BN heterostructure devices remain stable in air by encapsulating unstable phosphorene.[61] Additionally, h-BN, being a wide-bandgap insulator,[62] has a minimal impact on the topological properties of $MnBi_2Te_4$. Further, to realize interlayer FM coupling, distinct 3d orbital occupations in different SLs of $MnBi_2Te_4$ must arise through varying charge transfer between the upper and lower h-BN layers and the adjacent $MnBi_2Te_4$ layer in a stacked configuration. It is noteworthy that identical stacking arrangements between the upper h-BN/$MnBi_2Te_4$ and the lower $MnBi_2Te_4$/h-BN would result in nearly identical 3d orbital occupations in the two different SLs of $MnBi_2Te_4$, due to comparable charge transfer. Such configurations correspond to the sandwich structure h-BN/$MnBi_2Te_4$/h-BN, constructed by inserting 2-SL of $MnBi_2Te_4$ into an AA-stacked h-BN bilayer without ferroelectric polarization [see Figs. 1(b) and 1(e)]. Therefore, different stacking sandwich structures between the upper h-BN/$MnBi_2Te_4$ and the lower $MnBi_2Te_4$/h-BN must be considered, which is achievable by inserting 2-SL of $MnBi_2Te_4$ into AB [see Figs. 1(c) and 1(f)] or BA [see Figs. 1(d) and 1(g)] stacked h-BN bilayers with distinct ferroelectric polarizations. Meanwhile, a nonvolatile intrinsic electric field is induced in these sandwich heterostructures due to the broken inversion symmetry associated with the opposite ferroelectric polarizations, which might potentially enhance the magnetic anisotropy of the 2-SL $MnBi_2Te_4$.

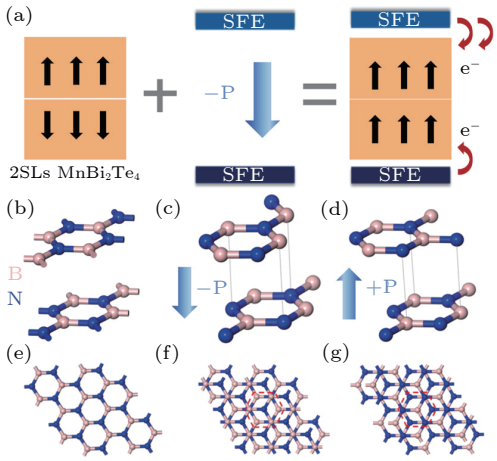

Fig. 1. (a) Schematic of the h-BN/$MnBi_2Te_4$/h-BN sandwich structure, constructed by a sliding ferroelectric (SFE) h-BN bilayer and a 2-SL $MnBi_2Te_4$ layer. A built-in electric field is formed due to distinct charge transfer between the upper and lower h-BN layers and the adjacent $MnBi_2Te_4$ layer. The black arrows indicate the magnetic moment direction of Mn atoms, the blue arrows denote the polarization direction of the SFE h-BN bilayer, and the red curved arrows depict charge transfer between h-BN and the adjacent $MnBi_2Te_4$. (b) Side view of an AA-stacked h-BN bilayer without ferroelectric polarization. (c) Side view of the h-BN bilayer with AB stacking and downward polarization after Moiré-engineering sliding. (d) Side view of the h-BN bilayer with BA stacking and upward ferroelectric polarization. (e)–(g) Top views of (b)–(d), respectively.

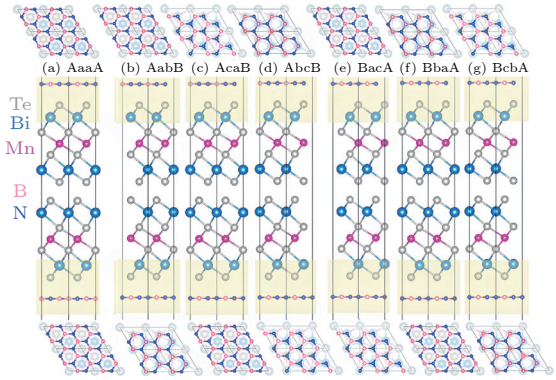

Fig. 2. Various stacking configurations are illustrated in the h-BN/2-SL $MnBi_2Te_4$/h-BN sandwich heterostructure. (a) Side view of the AaaA stacking configuration. (b)–(d) Top and side views of three representative stacking configurations within the downward-polarized (AB stacking) sandwich structure. (e)–(g) Top and side views of three representative stacking configurations within the downward-polarized (BA stacking) sandwich structure. Here, capital letters A or B indicate the stacking relationship between the upper and lower h-BN layers. Lowercase letters a, b, and c describe the stacking positions between the h-BN monolayer and the adjacent one-SL $MnBi_2Te_4$. Specifically, lowercase a denotes the B_hN_h stacking configuration, where both boron and nitrogen atoms of the h-BN monolayer are located at the hollow sites of the adjacent one-SL $MnBi_2Te_4$. Lowercase b refers to the B_hN_t stacking configuration, where the boron atoms occupy hollow sites within the adjacent one-SL $MnBi_2Te_4$, and the nitrogen atoms are located atop the Bi/Te atoms. Lowercase c indicates the B_tN_h stacking configuration, where the boron atoms are located atop the Bi/Te atoms, while the nitrogen atoms occupy the hollow sites of the adjacent one-SL $MnBi_2Te_4$. Element names are highlighted using the corresponding colored fonts for clarity.

Based on the aforementioned design principle, we proceed to elucidate the detailed stacking arrangements of the h-BN/$MnBi_2Te_4$/h-BN heterostructure in the subsequent section. Currently, both experimental and theoretical studies have confirmed the realization of sliding ferroelectricity with out-of-plane polarization in h-BN bilayers through Moiré engineering, owing to broken inversion symmetry.[63,64] SFE h-BN bilayers exhibit upward and downward polarizations, denoted as AB and BA stackings, respectively. When 2-SL of $MnBi_2Te_4$ is inserted into the h-BN bilayer with out-of-plane polarization, as illustrated in Figs. 2(b)–2(g), three stable stacking configurations [Figs. 2(b)–2(d)] for h-BN with downward polarization (AB stacking), and three stable configurations [Figs. 2(e)–2(g)] for h-BN with upward polarization (BA stacking), can be achieved by adjusting the relative positions between $MnBi_2Te_4$ and h-BN. In the six stable configurations, capital letters A or B represent the stacking relationship between the upper or lower h-BN layers, while lowercase letters a, b, or c indicate the stacking positions between the h-BN monolayer and the adjacent one-SL $MnBi_2Te_4$. Specifically, lowercase a denotes the B_hN_h stacking configuration, where both boron and nitrogen atoms of the h-BN monolayer reside in the hollow sites of the adjacent one-SL $MnBi_2Te_4$. Lowercase b rep-

resents the B_hN_t stacking configuration, where the boron atoms are situated at the hollow sites of the adjacent one-SL $MnBi_2Te_4$, and the nitrogen atoms occupy the top sites of the Bi/Te atoms. Similarly, lowercase c denotes the B_tN_h stacking configuration, where the boron atoms are located atop the Bi/Te atoms, while the nitrogen atoms reside in the hollow sites. Six configurations, AabB, AcaB, AbcB, BacA, BbaA, and BcbA, are thus constructed. For comparison, as shown in Fig. 2(a), a nonpolar AA-stacking configuration named AaaA is also provided.

Next, we evaluate the relative stability of the above seven configurations constructed by inserting 2-SL of $MnBi_2Te_4$ into an h-BN bilayer. In Fig. 3(a), the energy of the AaaA configuration with interlayer AFM coupling is set as the reference value (zero). The relative energies of all studied configurations with interlayer AFM and FM coupling are shown in Fig. 3(a). For the AB-stacked h-BN bilayer with downward ferroelectric polarization, the AabB configuration with interlayer FM coupling emerges as the most stable, being 0.03 meV and 7.17 meV lower than the AcaB and AbaB configurations, respectively. Conversely, for the BA-stacked h-BN bilayer with upward ferroelectric polarization, the BacA configuration with interlayer FM coupling is the most stable, being 8.82 meV and 14.80 meV lower than the BbaA and BcbA configurations, respectively.

In Fig. 3(b), the energy differences between the FM and AFM states of the seven configurations are calculated. For 2-SL of $MnBi_2Te_4$, our calculations show interlayer AFM coupling, consistent with a previous study.[65] When the 2-SL of $MnBi_2Te_4$ is inserted into the AA-stacked h-BN bilayer (AaaA configuration), the calculated results indicate that a transition from interlayer AFM coupling to FM coupling cannot occur due to the preserved symmetry of the system. It is noted that a previous calculation also showed that interlayer AFM coupling remains stable in h-BN/2-SL $MnBi_2Te_4$ heterostructures with similar stacking arrangements.[66] However, different behavior emerges when the 2-SL of $MnBi_2Te_4$ is inserted into AB- or BA-stacked h-BN bilayers. For the AB-stacked h-BN bilayer, the $E_{FM} - E_{AFM}$ values for the AabB, AcaB, and AbcB configurations are −5.44, −7.00, and 2.71 meV, respectively. Similarly, the values for BacA, BbaA, and BcbA are −16.90, 0.06, and −2.22 meV, respectively. Based on these results, the BacA configuration with interlayer FM coupling is the most stable structure for the upward-polarized h-BN/$MnBi_2Te_4$/h-BN heterostructures, exhibiting the strongest interlayer FM coupling among all configurations. To further assess the thermal stability of these FM states, we estimated the corresponding Curie temperatures T_C using the mean-field approximation formula $k_BT_C = -2\Delta E/3N$, where k_B is the Boltzmann constant, $\Delta E = E_{FM} - E_{AFM}$ is the magnetic energy difference, and N is the number of Mn atoms in the supercell. The estimated T_C values for AabB, AcaB, BacA, and BcbA are 21.0, 27.1, 65.4, and 8.6 K, respectively. Consistently, the BacA structure shows the highest T_C, further confirming its robust interlayer FM order.

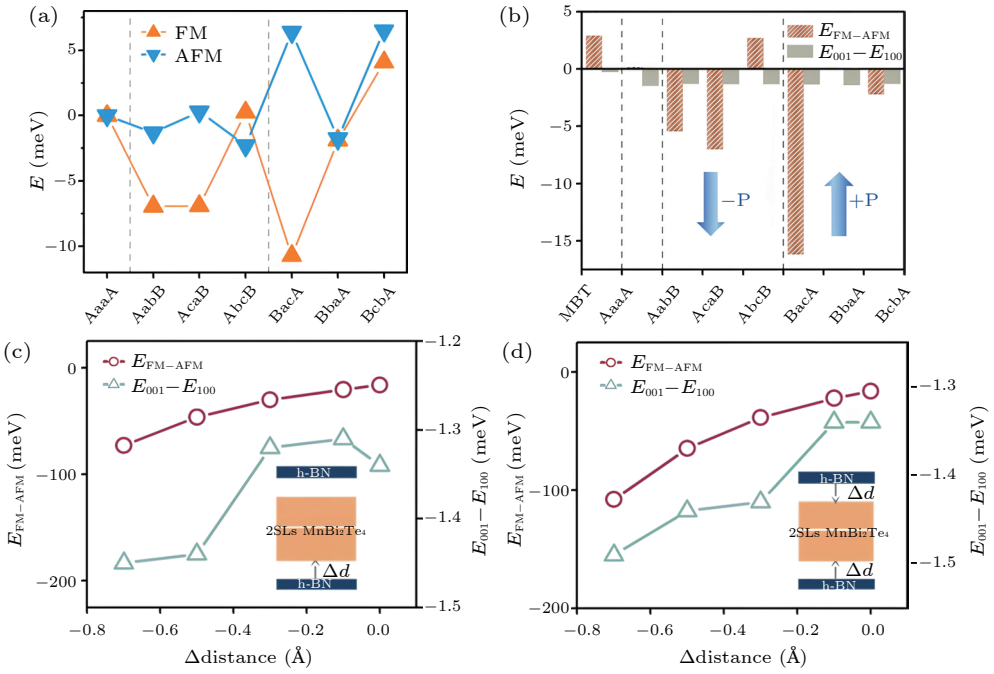

Fig. 3. (a) The relative stability of seven configurations constructed by inserting 2-SL of $MnBi_2Te_4$ into an h-BN bilayer. The energy of the AaaA configuration with interlayer AFM coupling is set as the reference (zero), and the relative energies of all studied configurations with both interlayer AFM and FM couplings are presented. (b) E_{FM-AFM} and $E_{001-100}$ energies, where negative values indicate a tendency toward interlayer FM coupling or out-of-plane magnetic anisotropy. (c) E_{FM-AFM} and $E_{001-100}$ energies under z-axis compressive strain by decreasing one of the interlayer distances between h-BN and the adjacent $MnBi_2Te_4$. (d) E_{FM-AFM} and $E_{001-100}$ energies under z-axis compressive strain when both interlayer distances between h-BN and adjacent $MnBi_2Te_4$ are simultaneously reduced.

Notably, a recent theoretical study found that interlayer AFM coupling can be weakened, or weak interlayer FM coupling can be achieved, by constructing heterostructures of $MnBi_2Te_4$ with ferroelectric materials such as In_2Se_3 or In_2Te_3.[67,68]

To improve the observation temperature and precision of the QAHE, experimental results have confirmed that magnetic fluctuations in $MnBi_2Te_4$ films can be suppressed by increasing magnetic anisotropy with the help of an external magnetic field. In this study, the MAE is defined as the energy difference between the out-of-plane and in-plane magnetization directions, denoted as $E_{[001]-[100]}$. A negative MAE indicates out-of-plane magnetic anisotropy, where the easy magnetization axis lies along the out-of-plane direction. For 2-SL of $MnBi_2Te_4$, the MAE is approximately -0.2 meV, consistent with earlier theoretical studies.[45] For the studied h-BN/$MnBi_2Te_4$/h-BN heterostructures, we find that the MAEs consistently increase from -0.2 meV to -1.4 meV, while the easy magnetization axis remains out-of-plane, which is beneficial for significantly enhancing the QAHE observation temperature. To understand the microscopic origin of this enhancement, we performed an orbital-resolved MAE analysis by comparing the SOC energies for different magnetization directions, as shown in Fig. S1 of SM. In pristine 2-SL of $MnBi_2Te_4$, the MAE is relatively weak, showing only a slight preference for out-of-plane magnetization, primarily originating from SOC interactions between the d_{yz} and d_{z^2} orbitals of Mn atoms. In contrast, the BacA heterostructure exhibits a significantly enhanced MAE, dominated by Mn d-orbital couplings, with a magnitude nearly three orders larger than that of pristine $MnBi_2Te_4$. Two competing orbital channels are identified: the d_{xy}–$d_{x^2-y^2}$ coupling favors in-plane magnetization (positive MAE), while the d_{yz}–d_{z^2} coupling favors out-of-plane magnetization (negative MAE). Although both channels are active, the out-of-plane contributions are stronger in the heterostructure, resulting in a pronounced enhancement of perpendicular magnetic anisotropy, thereby strengthening the out-of-plane magnetic stability of the system.

The distinct charge transfer between the upper and lower h-BN layers and the adjacent $MnBi_2Te_4$ layers in a stacked configuration notably influences interlayer magnetic coupling and the MAE of the investigated h-BN/$MnBi_2Te_4$/h-BN heterostructures. We hypothesize that reducing the interlayer distance between h-BN and the adjacent $MnBi_2Te_4$ through compressive strain should enhance both the interlayer magnetic coupling and the MAE due to the increased charge transfer. To test this hypothesis, we calculated the effects of compressive strain on $E_{\mathrm{FM-AFM}}$ and $E_{[001]-[100]}$ for the most stable BacA configuration, which exhibits the maximum FM stability. In Fig. 3(c), we first decrease one of the interlayer distances between h-BN and the adjacent $MnBi_2Te_4$. When the distance is reduced from the initial 3.6 Å to 3.5, 3.3, 3.1, and 2.9 Å, respectively, the $E_{\mathrm{FM-AFM}}$ increases from -16.19 meV to -20.15, -30.04, -46.31, and -72.99 meV, and the MAE also increases from the initial -1.34 meV to -1.45 meV. More pronounced improvements in magnetic properties occur when both interlayer distances are simultaneously compressed. As shown in Fig. 3(d), $E_{\mathrm{FM-AFM}}$ increases from -16.19 meV to -107.82 meV, approximately six times larger, and the MAE increases from the initial value of -1.34 meV to -1.49 meV, while maintaining the out-of-plane easy magnetization axis when the interlayer distance is reduced from 3.6 Å to 2.9 Å. Thus, our results demonstrate that applied z-axis compressive strain not only significantly enhances the interlayer FM coupling strength but also increases the out-of-plane magnetic stability, which is beneficial for enhancing the experimental observation temperature and precision of the QAHE.

What is the underlying magnetic mechanism in h-BN/$MnBi_2Te_4$/h-BN heterostructures? Previous studies have found that distinct 3d orbital occupations emerge in the 2-SL of $MnBi_2Te_4$.[45] In our system, this can be attributed to the asymmetric charge transfer between the upper and lower h-BN layers and the adjacent $MnBi_2Te_4$ layers in the stacked heterostructure. To verify this mechanism, we take the BacA configuration as an example and calculate the differential charge density using the following expression:

$$\Delta\rho = \rho_{\mathrm{total}} - \rho_{\mathrm{upper\ h\text{-}BN}} - \rho_{\mathrm{upper\ SL\ MnBi_2Te_4}} - \rho_{\mathrm{lower\ SL\ MnBi_2Te_4}} - \rho_{\mathrm{lower\ h\text{-}BN}}\,.$$

For comparative analysis, the differential charge density is also presented for the interlayer AFM-coupled AaaA configuration, as shown in Fig. 4. As illustrated in Figs. 4(a) and 4(e), the charge accumulation and depletion at the interfaces of the upper h-BN/$MnBi_2Te_4$ and the lower $MnBi_2Te_4$/h-BN are nearly identical due to the preserved inversion symmetry in the AaaA configuration, leading to nearly the same 3d orbital occupations in each SL of $MnBi_2Te_4$. This is evident from the charge distribution around Mn atoms, where the upper SL mirrors the lower SL, as shown in Figs. 4(c) and 4(g). Thus, the AaaA configuration is characterized by interlayer AFM coupling, which may also relate to a previous study showing that only interlayer AFM coupling is stable in h-BN/2-SL $MnBi_2Te_4$ heterostructures with symmetric stacking.[66] However, for the BacA configuration with broken inversion symmetry, as depicted in Figs. 4(b) and 4(f), significantly different patterns of charge accumulation and depletion appear at the two interfaces, which strongly affect the 3d orbital occupations in each SL of $MnBi_2Te_4$. As demonstrated in Figs. 4(d) and 4(h), the charge distribution around Mn atoms in the upper SL differs significantly from that in the lower SL. These distinct charge redistributions around Mn atoms in the 2-SL introduce new hopping channels between the upper and lower Mn atoms in the h-BN/2-SL $MnBi_2Te_4$/h-BN heterostructure and lead to a magnetic phase transition from interlayer AFM to FM coupling.

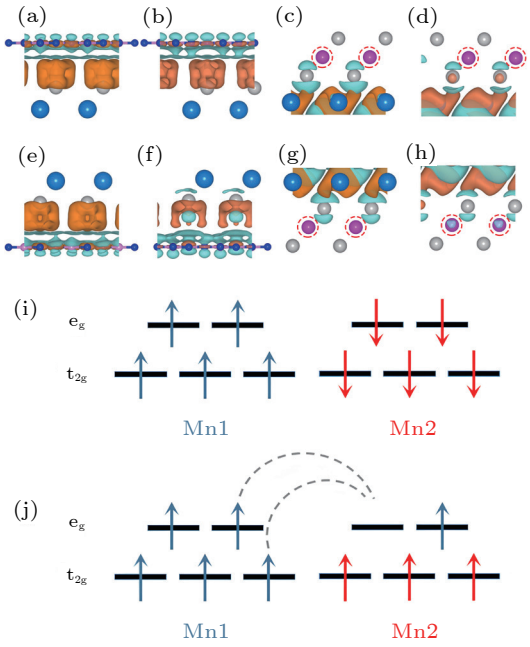

Fig. 4. (a), (e), and (b), (f) The difference charge density between the upper and lower interfaces of h-BN and the adjacent $MnBi_2Te_4$ in the AaaA and BacA sandwich structures, where orange signifies charge accumulation and cyan indicates charge depletion. (c), (g), and (d), (h) The difference charge density maps near Mn atoms in the upper $MnBi_2Te_4$ and lower $MnBi_2Te_4$ regions of the AaaA and BacA sandwich structures. The Mn atom positions are marked with red dashed circles. (i) Schematic representation of the AFM configuration of Mn1 and Mn2 in the initial state of the 2-SL $MnBi_2Te_4$, where the ferromagnetic configuration is prohibited by Hund's rule. (j) Schematic representation of the exchange interaction between Mn1's e_g t_{2g} and Mn2's e_g t_{2g} orbitals in the BacA sandwich structure. The reduction in the occupancy of Mn2's d orbitals creates new transition pathways between Mn1 and Mn2.

The above mechanism of the magnetic phase transition from interlayer AFM to FM coupling is schematically represented in Figs. 4(i) and 4(j). Mn^{2+} ions have a $3d^5 4s^0$ electron configuration. Due to strong Hund's rule coupling, all five electrons occupy the same spin (e.g., spin-up), leaving the opposite spin (spin-down) completely empty. In the AFM state of 2-SL $MnBi_2Te_4$, electron transitions between spin-up d orbitals of adjacent Mn atoms are allowed, as both the t_{2g} and e_g orbitals are fully occupied in the same spin channel. These allowed transitions facilitate superexchange interactions, stabilizing the AFM ground state. However, in the FM state, transitions between e_g and t_{2g} orbitals are prohibited by Hund's rules, which favor AFM coupling in 2-SL $MnBi_2Te_4$. In our h-BN/2-SL $MnBi_2Te_4$/h-BN system, Figure 4(j) illustrates the exchange interactions between Mn atoms in the upper and lower SLs in the BacA structure, where Mn1 denotes the Mn atom in the top SL and Mn2 denotes the Mn atom in the bottom SL. To further elucidate the interlayer exchange mechanism, we calculated the integrated density of states of the Mn d orbitals for Mn1 and Mn2 in the BacA configuration. As shown in Fig. S2 of SM, the total d-orbital occupation of Mn1 is significantly higher than that of Mn2, with an occupation difference of $\Delta N = 1.25$. This orbital asymmetry facilitates interlayer exchange processes, particularly from Mn1's e_g to Mn2's e_g orbitals and from Mn1's t_{2g} to Mn2's e_g orbitals, which in turn enables the emergence of interlayer FM coupling between the two layers.

To determine whether our proposed sandwich heterostructures with interlayer FM coupling can realize the QAHE, we analyzed the band structures and topological properties of the BacA configuration. From Fig. 5(a), it is evident that the band structure exhibits a gap of 53.28 meV at the Dirac point Γ, indicating an insulating bulk state. Atomic orbital analysis reveals contributions from Te p orbitals in the conduction band and Bi p orbitals in the valence band, resulting in a band inversion at the Γ point and confirming the nontrivial topological nature of the band gap. We further confirmed the topology of the BacA heterostructure by integrating the Berry curvature over the occupied valence bands. Figure 5(b) shows the Berry curvature distribution along high-symmetry paths, featuring a sharp peak at the Γ point and vanishing elsewhere. This implies that the total Berry curvature integral, or equivalently the Hall conductivity, is nonzero near the Fermi level. A nonzero Berry curvature indicates the presence of a transverse current, contributing to a quantized Hall conductivity of $+e^2/h$. Figure 5(c) presents the energy-dependent Hall conductivity σ_{xy}, which exhibits a quantized plateau of $+e^2/h$ near the Fermi level, corresponding to a Chern number of $C = 1$. Additionally, we used the WannierTools package to calculate the edge states of the system. As shown in Fig. 5(d), a chiral edge state traverses the bulk gap from the conduction to the valence band, crossing the Fermi level once, consistent with the Chern number $C = 1$. These results collectively demonstrate that the designed h-BN/$MnBi_2Te_4$/h-BN sandwich heterostructure with interlayer FM coupling is a promising candidate for realizing high-temperature QAHE with a large nontrivial energy gap. Notably, a recent experimental study observed QAHE at zero magnetic field in AlO_x-capped $MnBi_2Te_4$, attributed to enhanced surface magnetism provided by the AlO_x capping layer.[69]

In summary, based on first-principles calculations, we propose a practical and effective approach to manipulate the interlayer magnetic coupling in the intrinsic TI $MnBi_2Te_4$ using a capped sliding vdW material. Our results indicate the following: (I) In the h-BN/2-SL $MnBi_2Te_4$/h-BN system, most stacking configurations undergo a transition from interlayer AFM to FM coupling, and the MAE with an out-of-plane easy magnetization axis is significantly enhanced. (Ⅱ) Compressive strain along the z-axis can further strengthen both the interlayer FM coupling and the out-of-plane MAE. (Ⅲ) The band structure of the most stable h-BN/2-SL $MnBi_2Te_4$/h-BN heterostructure exhibits a nontrivial topological band gap of approximately 53 meV, corresponding to a Chern number of $C = 1$, indicating the realization of the QAHE. Our proposed scheme not only enables interlayer FM coupling but also takes advantage of the excellent chemical stability

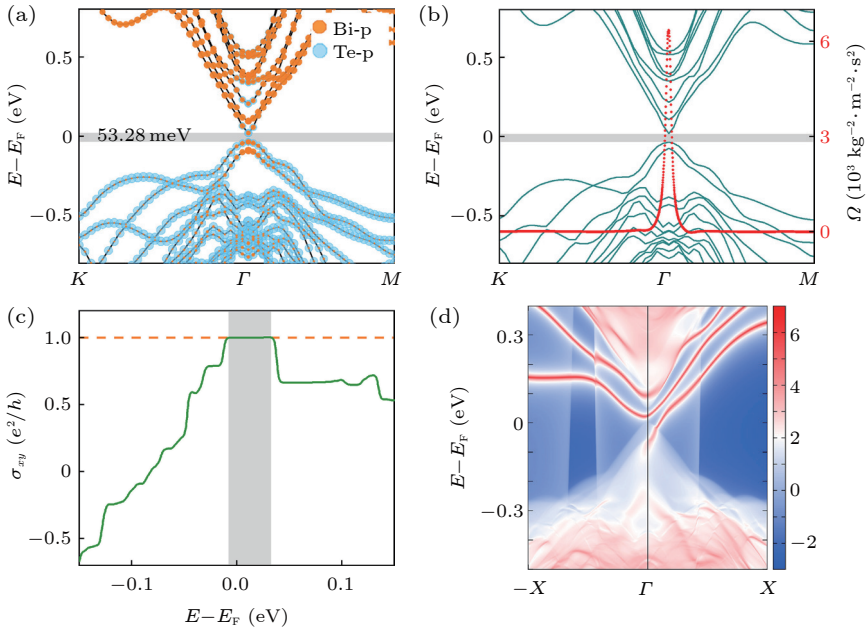

Fig. 5. (a) Band structure of the BacA sandwich heterostructure along the high-symmetry line with the band gap indicated by shading. The corresponding Berry curvature distribution is presented in (b). (c) The Hall conductivity as a function of energy variation. (d) The gapless chiral edge surface states in the system.

of h-BN. Furthermore, this study provides a promising route to achieving high-temperature QAHE in $MnBi_2Te_4$ films and presents a new strategy for tuning the magnetic properties of 2D vdW magnetic materials via SFE engineering.

Acknowledgements. This work was supported by the National Key R&D Program of China (Grant No. 2024YFA1408103), National Natural Science Foundation of China (Grants No. 11974098, 12474158, 12234017 and 12488101), Innovation Program for Quantum Science and Technology (Grant No. 2021ZD0302800), Natural Science Foundation of Hebei Province (Grant No. A202305017), Anhui Initiative in Quantum Information Technologies (Grant No. AHY170000), and Fundamental Research Funds for the Central Universities (Grant No. WK2340000082). The Supercomputing services of University of Science and Technology of China are gratefully acknowledged.

References

[1] Ren Y, Qiao Z, and Niu Q 2016 *Rep. Prog. Phys.* **79** 066501
[2] He K, Wang Y, and Xue Q K 2018 *Annu. Rev. Condens. Matter Phys.* **9** 329
[3] Hasegawa S 2025 *Coshare Science* **03** 01
[4] Haldane F D M 1988 *Phys. Rev. Lett.* **61** 2015
[5] Novoselov K S, Geim A K, Morozov S V, Jiang D, Zhang Y, Dubonos S V, Grigorieva I V, and Firsov A A 2004 *Science* **306** 666
[6] Wu S C, Shan G, and Yan B 2014 *Phys. Rev. Lett.* **113** 256401
[7] Yu R, Zhang W, Zhang H J, Zhang S C, Dai X, and Fang Z 2010 *Science* **329** 61
[8] Mogi M, Yoshimi R, Tsukazaki A, Yasuda K, Kozuka Y, Takahashi K, Kawasaki M, and Tokura Y 2015 *Appl. Phys. Lett.* **107** 182401
[9] Jiang H, Qiao Z, Liu H, and Niu Q 2012 *Phys. Rev. B* **85** 045445
[10] Qiao Z, Ren W, Chen H, Bellaiche L, Zhang Z, MacDonald A H, and Niu Q 2014 *Phys. Rev. Lett.* **112** 116404
[11] Onoda M and Nagaosa N 2003 *Phys. Rev. Lett.* **90** 206601
[12] Qiao Z, Yang S A, Feng W, Tse W K, Ding J, Yao Y, Wang J, and Niu Q 2010 *Phys. Rev. B* **82** 161414
[13] Qi S, Gao R, Chang M, Han Y, and Qiao Z 2020 *Phys. Rev. B* **101** 014423
[14] Qi S, Gao R, Chang M, Hou T, Han Y, and Qiao Z 2020 *Phys. Rev. B* **102** 085419
[15] Gao R, Qin G, Qi S, Qiao Z, and Ren W 2021 *Phys. Rev. Mater.* **5** 114201
[16] Liang W, Li Z, An J, Ren Y, Qiao Z, and Niu Q 2025 *Phys. Rev. Lett.* **134** 116603
[17] Li Z, Han Y, Liang W, and Qiao Z 2025 *Phys. Rev. B* **111** 115416
[18] Li X, Zhang H, Xu H, Sang H, Wang X, Qi S, and Qiao Z 2024 *Phys. Rev. B* **109** 155427
[19] Han Y, Pan S, and Qiao Z 2023 *Phys. Rev. B* **108** 115302
[20] Han Y, Yan Z, Li Z, Xu X, Zhang Z, Niu Q, and Qiao Z 2023 *Phys. Rev. B* **107** 205412
[21] Zhu X, Chen Y, Liu Z, Han Y, and Qiao Z 2023 *Front. Phys.* **18** 23302
[22] Li Z, Han Y, and Qiao Z 2022 *Phys. Rev. Lett.* **129** 036801
[23] Rehman M U, Dong X, Hou T, Li Z, Qi S, and Qiao Z 2019 *Phys. Rev. B* **100** 195422
[24] Deng X, Yang H, Qi S, Xu X, and Qiao Z 2018 *Front. Phys.* **13** 137308
[25] Deng X, Qi S, Han Y, Zhang K, Xu X, and Qiao Z 2017 *Phys. Rev. B* **95** 121410
[26] Qi S, Qiao Z, Deng X, Cubuk E D, Chen H, Zhu W, Kaxiras E, Zhang S B, Xu X, and Zhang Z 2016 *Phys. Rev. Lett.* **117** 056804
[27] Jiang G, Feng Y, Wu W, Li S, Bai Y, Li Y, Zhang Q, Gu L, Feng X, Zhang D, Song C, Wang L, Li W, Ma X C, Xue Q K, Wang Y, and He K 2018 *Chin. Phys. Lett.* **35** 076802
[28] Sui Q, Zhang J, Jin S, Xia Y, and Li G 2020 *Chin. Phys. Lett.* **37** 097301
[29] Cui Q, Liang J, Zhu Y, Yao X, and Yang H 2023 *Chin. Phys. Lett.* **40** 037502

[30] Wu X C, Li S Z, Si J S, Huang B, and Zhang W B 2024 *Chin. Phys. Lett.* **41** 057303
[31] Zhao J, Liu G B, Chen P, Yao Y, Zhang G, and Du L 2024 *Chin. Phys. Lett.* **41** 066801
[32] Qi X L and Zhang S C 2011 *Rev. Mod. Phys.* **83** 1057
[33] Liu F 2023 *Coshare Science* **01** 03
[34] Chang C Z, Zhang J, Feng X, Shen J, Zhang Z, Guo M, Li K, Ou Y, Wei P, Wang L L, Ji Z, Feng Y, Ji S, Chen X, Jia J, Dai X, Fang Z, Zhang S C, He K, Wang Y, Liu L, Ma X, and Xue Q K 2013 *Science* **340** 167
[35] Watanabe R, Yoshimi R, Kawamura M, Mogi M, Tsukazaki A, Yu X, Nakajima K, Takahashi K S, Kawasaki M, and Tokura Y 2019 *Appl. Phys. Lett.* **115** 102403
[36] Deng Y, Yu Y, Shi M Z, Wang J, Chen X H, and Zhang Y 2020 *Science* **367** 895
[37] Dong X, Jia X, Yan Z, Shen X, Li Z, Qiao Z, and Xu X 2023 *Chin. Phys. Lett.* **40** 087301
[38] Ji H R, Liu Y Z, Wang H, Luo J W, Li J H, Li H, Wu Y, Xu Y, and Wang J 2021 *Chin. Phys. Lett.* **38** 107404
[39] Serlin M, Tschirhart C L, Polshyn H, Zhang Y, Zhu J, Watanabe K, Taniguchi T, Balents L, and Young A F 2019 *Science* **367** 848
[40] Li T, Jiang S, Shen B, Zhang Y, Li L, Tao Z, Devakul T, Watanabe K, Taniguchi T, Fu L, Shan J, and Mak K F 2021 *Nature* **600** 641
[41] Li J, Li Y, Du S, Wang Z, Gu B L, Zhang S C, He K, Duan W, and Xu Y 2019 *Sci. Adv.* **5** eaaw5685
[42] Gong Y, Guo J, Li J, Zhu K, Liao M, Liu X, Zhang Q, Gu L, Tang L, Feng X, Zhang D, Li W, Song C, Wang L, Yu F, Chen X, Wang Y, Yao H, Duan W, Xu Y, Zhang S C, Ma X, Xue Q K, and He K 2019 *Chin. Phys. Lett.* **36** 076801
[43] Sun H, Xia B, Chen Z, Zhang Y, Liu P, Yao Q, Tang H, Zhao Y, Xu H, and Liu Q 2019 *Phys. Rev. Lett.* **123** 096401
[44] Ge J, Liu Y, Li J, Li H, Luo T, Wu Y, Xu Y, and Wang J 2020 *Nat. Sci. Rev.* **7** 1280
[45] Li Z, Li J, He K, Wan X, Duan W, and Xu Y 2020 *Phys. Rev. B* **102** 081107
[46] Zhu W, Song C, Liao L, Zhou Z, Bai H, Zhou Y, and Pan F 2020 *Phys. Rev. B* **102** 085111
[47] Fu H, Liu C X, and Yan B 2020 *Sci. Adv.* **6** eaaz0948
[48] Han Y, Sun S, Qi S, Xu X, and Qiao Z 2021 *Phys. Rev. B* **103** 245403
[49] You J Y, Dong X J, Gu B, and Su G 2021 *Phys. Rev. B* **103** 104403
[50] Cai J, Ovchinnikov D, Fei Z, He M, Song T, Lin Z, Wang C, Cobden D, Chu J H, Cui Y T, Chang C Z, Xiao D, Yan J, and Xu X 2022 *Nat. Commun.* **13** 1668
[51] Kresse G and Furthmuller J 1996 *Phys. Rev. B* **54** 11169
[52] Blöchl P E 1994 *Phys. Rev. B* **50** 17953
[53] Perdew J P, Burke K, and Ernzerhof M 1996 *Phys. Rev. Lett.* **77** 3865
[54] Li B, Pajerowski D M, Riberolles S X M, Ke L, Yan J Q, and McQueeney R J 2021 *Phys. Rev. B* **104** L220402
[55] Grimme S, Antony J, Ehrlich S, and Krieg H 2010 *J. Chem. Phys.* **132** 154104
[56] Steiner S, Khmelevskyi S, Marsmann M, and Kresse G 2016 *Phys. Rev. B* **93** 224425
[57] Otrokov M M, Menshchikova T V, ergniory M G V, Rusinov I P, Vyazovskaya A Y, Koroteev Y M, Bihlmayer G, Ernst A, Echenique P M, and Arnau A 2017 *2D Mater.* **4** 025082
[58] Mostofi A A, Yates J R, Lee Y S, Souza I, Vanderbilt D, and Marzari N 2008 *Comput. Phys. Commun.* **178** 685
[59] Wu Q, Zhang S, Song H F, Troyer M, and Soluyanov A A 2018 *Comput. Phys. Comm.* **224** 405
[60] Yang J, Wu B, Zhou J, Lu J, Yang J, and Shen L 2023 *Nanoscale* **15** 16103
[61] Gillgren N, Wickramaratne D, Shi Y, Espiritu T, Yang J, Hu J, Wei J, Liu X, Mao Z, and Watanabe K 2015 *2D Mater.* **2** 011001
[62] Kim S M, Hsu A, Park M H, Chae S H, Yun S J, Lee J S, Cho D -H, Fang W, Lee C, Palacios T, Dresselhaus M, Kim K K, Lee Y H, and Kong J 2015 *Nat. Commun.* **6** 8662
[63] Wang Y, Jiang S, Xiao J, Cai X, Zhang D, Wang P, Ma G, Han Y, Huang J, Watanabe K, Taniguchi T, Guo Y, Wang L, Mayorov A S, and Yu G 2022 *Front. Phys.* **17** 43504
[64] Jiang W, Liu C, Ma X, Yu X, Hu S, Li X, Burton L A, Liu Y, Chen Y, Guo P, Kong X, Bellaiche L, and Ren W 2022 *Phys. Rev. B* **106** 054104
[65] Wu J, Liu F, Sasase M, Ienaga K, Obata Y, Yukawa R, Horiba K, Kumigashira H, Okuma S, Inoshita T, and Hosono H 2019 *Sci. Adv.* **5** eaax9989
[66] Bosnar M, Vyazovskaya A Y, Petrov E K, Chulkov E V, and Otrokov M M 2023 *npj 2D Mater Appl* **7** 33
[67] Luo W, Du M H, Reboredo F A, and Yoon M 2023 *2D Mater.* **10** 035008
[68] Yu G, Tang C, Tian Z, Zhu Z, Liu P, Pan A, Chen M, and Chen X Q 2023 *Phys. Rev. B* **108** 014106
[69] Wang Y, Fu B, Wang Y, Lian Z, Yang S, Li Y, Xu L, Gao Z, Yang X, Wang W, Jiang W, Zhang J, Wang Y, and Liu C 2025 *Nat. Commun.* **16** 1727